

Skylon Aerospace Plane and Its Aerodynamics and Plumes

Unmeel Mehta,* Michael Aftosmis,[†] Jeffrey Bowles,[‡] and Shishir Pandya[§]
NASA Ames Research Center, Moffett Field, California 94035

DOI: 10.2514/1.A33408

The Skylon concept incorporates the highly innovative synergetic air-breathing rocket engine concept that has the potential to revolutionize the mode of propulsion for transportation of medium-weight payloads to low Earth orbits. An independent partial assessment is provided of the technical viability of the Skylon concept. Pressure lift and drag coefficients derived from Euler simulations for unpowered flight compare very well and fairly well, respectively, with those from engineering methods. The engineering-method coefficients for powered flight are increasingly less acceptable as the freestream Mach number is increased beyond 8.5 because these methods did not account for the increasing favorable (in terms of pressure forces) effect of underexpanded rocket engine plumes on the aft fuselage. At Mach numbers greater than 8.5, the thermal environment around the aft fuselage is a known unknown: a potential design and/or performance risk issue. The adverse effects of shock waves on the aft fuselage and plume-induced flow separation are other potential risks. A preliminary design of Skylon requires the judicious use of a combination of engineering methods, advanced methods based on required physics or analytical fidelity, test data, and independent assessments. The demonstration of a synergetic air-breathing rocket-engine-powered experimental aerospace plane calls for the second revival of the Aerospace Plane Program.

Nomenclature

A_e	=	nozzle exit area
A_t	=	nozzle throat area
C_D	=	pressure drag coefficient
C_L	=	pressure lift coefficient
C_z	=	pressure moment around the z axis
F_x	=	pressure force in the x direction, the direction from the nose to the tail of Skylon
F_y	=	pressure force in the y direction, the vertical direction
F_z	=	pressure force in the z direction, the spanwise direction
h	=	altitude
J	=	objective function
M_j	=	jet Mach number at nozzle exit
M_{LE}	=	wing leading-edge Mach number
M_∞	=	freestream Mach number
m_a	=	airflow rate
m_e	=	mass flow rate at nozzle exit
m_f	=	fuel flow rate
P_e	=	static pressure at nozzle exit
P_{1t}	=	total pressure at the exit of combustion chamber
p_∞	=	freestream pressure
T_e	=	static temperature at nozzle exit
T_{rec}	=	freestream recovery temperature
T_{tot}	=	freestream total temperature
T_{1t}	=	total temperature at the exit of combustion chamber
V_e	=	velocity at nozzle exit
α_f	=	foreplane angle of attack

α_v	=	vehicle angle of attack
γ_j	=	ratio of specific heat γ at the nozzle exit

I. Introduction

SERIOUS efforts began in 1958 to develop a reusable launch vehicle (RLV) for transportation to low Earth orbit (LEO) with the start of the Aerospaceplane program [1,2]. In 1970, when the U.S. Space Shuttle Phase B award began, NASA and contractors were generally unanimous in considering a two-stage-to-orbit (TSTO) reusable launch system (RLS) powered with rocket engines as the system of choice [3,4]. However, the design was changed to fit the budget, and the full reusability requirement was dropped [4,5]. Subsequently, substantial efforts to develop reusable launchers were pursued in endeavors such as the National Aero-Space Plane (NASP), horizontal takeoff and landing (HOTOL), Sänger II, X-33/VentureStar, and Skylon. Almost all RLV and RLS efforts were terminated, the reasons for which are highlighted later. Only the Skylon endeavor is ongoing, principally because the conceptual design of Skylon incorporates potential breakthrough propulsive advances. Those failures and advances provide the rationale for the assessment effort undertaken here. The specific motivation and objectives for this work are stated at the end of this section.

The Aerospaceplane program (1958–1964) was initiated to develop a single-stage-to-orbit (SSTO) aerospace plane powered by an air-breathing engine. Numerous launch configurations were investigated. The program evolved into the recoverable orbital launch system (ROLS), an SSTO vehicle [2]. The ROLS had a complicated and badly conceived [6] propulsion system: a liquid air collection engine system, which was later renamed the air collection and enrichment system. When the feasibility of the SSTO design became uncertain, the focus shifted to TSTO system concepts. The selected TSTO system corresponded closely to Sänger II [1]. The program technology effort focused on the construction of a scramjet engine to be launched on top of a missile [7]. The U.S. Air Force Scientific Advisory Board condemned the program and asserted the following: “The so-called Aerospaceplane program has had such an erratic history, has involved so many clearly infeasible factors, . . . It is also recommended that the Air Force increase the vigilance that no new program achieves such a difficult position” [6].

The NASP program (1986–1995) was planned to build and flight test a manned experimental vehicle, the X-30, to validate technologies. The disciplines of propulsion, structures, and aerodynamics were highly coupled. New technologies related to air-breathing scramjets and combined-cycle engines, new materials, a new design process, and advances in computational fluid dynamics (CFD) for credible

Presented as Paper 2015-3605 at the 20th AIAA International Space Planes, Hypersonic Systems and Technologies Conference, University of Strathclyde, Glasgow, Scotland, U.K., 6–9 July 2015; received 5 August 2015; revision received 24 November 2015; accepted for publication 27 November 2015; published online 25 February 2016. This material is declared a work of the U.S. Government and is not subject to copyright protection in the United States. Copies of this paper may be made for personal and internal use, on condition that the copier pay the per-copy fee to the Copyright Clearance Center (CCC). All requests for copying and permission to reprint should be submitted to CCC at www.copyright.com; employ the ISSN 0022-4650 (print) or 1533-6794 (online) to initiate your request.

*Aerospace Engineer, NASA Advanced Supercomputing Division; Unmeel.B.Mehta@nasa.gov. Associate Fellow AIAA.

[†]Aerospace Engineer, Applied Modeling and Simulation Branch; Michael.Aftosmis@nasa.gov. Associate Fellow AIAA.

[‡]Aerospace Engineer, System Analysis Branch; Jeffrey.V.Bowles@nasa.gov.

[§]Aerospace Engineer, Fundamental Modeling and Simulation Branch; Shishir.Pandya@nasa.gov. Senior Member AIAA.

simulations were required. Although tremendous advances were made in technology, its overall goal, an SSTO RLV for space access, was very difficult to achieve. As designed, the X-30, with an arbitrary takeoff gross weight limit, was unable to achieve the SSTO goal, after approximately \$2.86 billion [8] was spent.

The integrated air-breathing engine for the X-30 was to operate in three modes: low speed ($M_\infty = 0$ to ~ 3), ramjet ($M_\infty = \sim 3$ to ~ 6), and scramjet ($M_\infty = \sim 6$ to ~ 16). Rocket propulsion was used to achieve orbit. External burning was used to reduce the drag created by the X-30's nozzle at lower speeds. Engine tests demonstrated that the engine design looked promising at high speeds, but it did not produce sufficient thrust at lower speeds [8]. The proposed integrated propulsion system presented unprecedented challenges. "Perhaps the highest technical risk in the program is the ability to quantify the characteristics of the scramjet and its flowpath integration into the airplane" [9]. Whether the goal of SSTO was worth pursuing on its own merit was also questioned [8]. The RAND Corporation also believed that a TSTO concept close to S nger II should be a strong contender for the NASP program [1]. Subsequently, additional efforts were conducted to develop a TSTO RLS with air-breathing propulsion on the first stage [10–18].

A way to increase the Mach range of air-breathing propulsion is to use a turbine-based combination cycle (TBCC) engine, which is designed either with a turbine or turbo ramjet engine (for example, the PW-J58 engine) plus a dual-mode ramjet (or ramjet–scramjet) engine. Ideally, a dual-mode ramjet engine would nominally start in ramjet mode at $M_\infty = 3$, then transition from ramjet mode to scramjet mode around $M_\infty = 7$, and finally perform in scramjet mode until $M_\infty \sim 14$ (above which rocket performance is superior).

Separated, the ramjet and scramjet technologies are relatively easier than the dual-mode technology. Under ramjet power, the seventh flight of the Advanced Strategic Air-Launched Missile and the fourth flight of the X-51A missile flew, respectively, at $M_\infty = 4$ for 290 and for 210 s reaching a peak speed of Mach 5.1 after being launched at $M_\infty \sim 4.8$. The X-43A aircraft was propelled with a scramjet engine twice, achieving, in flights 2 and 3, Mach 6.83 and 9.68, respectively [19]. The Hypersonic International Flight Research Experimentation (HIFIRE) program [20] also flew a scramjet engine in flight 3. HIFIRE flight 2 has demonstrated mode transition from ramjet to scramjet from Mach 6 to Mach 8+ [21]. Each of these flights lasted less than 15 s. Such efforts are essential for developing operational missiles and for high-speed flight research.

Over the last 55-plus years, there has been a lack of progress in developing an operational dual-mode ramjet engine across a wide freestream Mach number range. Likewise, the aforementioned TBCC engine has yet to be demonstrated in continuous operation over a meaningful Mach number range.

Without a ground-based test facility for testing a dual-mode ramjet or a TBCC engine across a Mach number range of interest during a single test run, the development effort for such engines is difficult. The size of the tested engine and the test environment need to be appropriate. The absence of long-duration, clean-air, true-enthalpy, high-Mach-number testing capability is a serious issue for developing high-Mach-number scramjet technology. For example, such a capability is required to ascertain structural response to scramjet aerothermal environments. Thus, the development of an operational dual-mode scramjet that operates from $M_\infty \sim 3$ to ~ 16 is extremely difficult compared to the task of extending the maximum operational Mach number of turbine engines from $M_\infty \sim 2.5$ to ~ 5.5 with precompressor cooling. The use of a turbine engine operating up to $M_\infty \sim 5.5$ allows the start of a dual-mode scramjet at $M_\infty \sim 5$ in a TBCC engine.

The limitations of ground-test facilities and those of computational design tools, the highly integrated nature of the air-breathing propulsion system operating from Mach 0 to ~ 16 , and numerous examples of flight data being at variance with ground-test data and computed results make flight tests essential. The requirements for developing this propulsion system dictate flight tests of near-full-scale vehicles, corresponding to the desired prototype or operational plane [22]. However, flight tests can be risky, and they are expensive.

The integration of a turbine engine with a dual-mode ramjet engine can be avoided if different propulsion systems are in separate

vehicles. For example, a four-stage RLS could be used to launch small satellites [23,24]. A subsonic carrier aircraft carries a two-stage system and launches it. This system consists of the second stage, a supersonic aircraft, and the third stage, a hypersonic aircraft. The third stage is in tandem with the second stage. The hypersonic aircraft carries the fourth stage internally. This stage is powered with a rocket engine and carries the payload. All stages are recovered for future use. Another approach is to launch an expandable, rocket-powered multistaged system at a subsonic Mach number from an aircraft [25–27]. Both of these approaches have the potential to reduce current launch costs, but they are not satisfactory for commercializing LEO.

S nger II was only a guiding reference concept for the German Hypersonic Technology Program (1988–1993) [28]. It was designed as a TSTO RLS concept because of a firm conviction that SSTO RLVs were not practical. The first stage and the second stage were, respectively, powered by a turbo ramjet combined cycle engine and rocket engines. The first stage was designed to cruise and could be evolved into a hypersonic aircraft. The second stage was a winged vehicle. Conceptually, it was staged at $M_\infty = 6.6$. The Hypersonic Technology Program also included the development and test of a subscale flight demonstrator to validate the design and propulsion system of the first stage. A concentric propulsion system with the turbojet in the middle and the ramjet surrounding it (a coaxial turbo ramjet engine) was chosen [29,30]. In 1994, the S nger II technology and development effort was canceled because it would have been very costly and because the first-generation system would reduce the launch cost only between 10 and 30% below that of the Arian 5 ELV [31].

The X-33 program (1996–2001) was to pave the way to VentureStar, an SSTO RLV. The X-33 reusable launcher was a subscale, unmanned technology demonstrator powered with rocket engines. It was designed to achieve $M_\infty \sim 13$ and to land horizontally like an airplane. The X-33 program experienced difficulties achieving its goals primarily because realistic cost estimates, timely acquisition and risk management plans, and adequate and realistic performance goals were not developed [32]. During its life, \$1.27 billion was expended [33].

Because SSTO RLVs were not feasible with rocket engines, the basic idea for the SSTO HOTOL vehicle (1982–1989) was to augment rocket engine performance using the atmosphere instead of starting with an air-breathing engine, and then to find some way to add a rocket engine for the latter part of the flight [34]. This approach was used to design the HOTOL propulsion system, the Rolls Royce RB545 engine, which was a combined-cycle precooled engine [35].

The conceptual, unpowered, reusable Skylon aerospace plane (1989 to present), an SSTO RLV, which can be used as a reusable first stage of a TSTO launch system ([36] pp. 35–39), evolved from HOTOL. For this concept, various propulsion concepts, hydrogen/oxygen rockets, scramjets, turbojets, turbo rockets, and liquid air cycle engines, were considered [37]. The conceptual Synergistic Air-Breathing Rocket Engine (SABRE) was specifically designed to combine some of the best features of the considered concepts while simultaneously overcoming their faults. This combined-cycle engine (Fig. 1) is a highly innovative concept; the engine operates in the

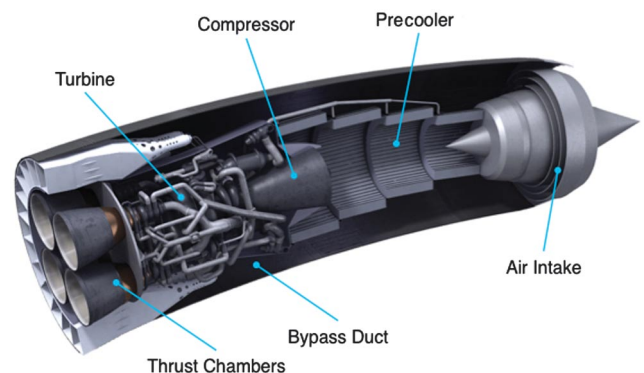


Fig. 1 Synergistic air-breathing rocket engine (courtesy of Reaction Engines Limited).

turbine, turboramjet, or rocket mode. Ground testing and development of this engine, having relevant size and desired performance, is feasible at sea-level static conditions.

The foremost enabling technology in SABRE is the demonstrated heat exchanger technology [38–41]. This technology is essential to significantly expand the operational envelope of conventional turbine engines by precooling hot ram-compressed air at high speeds. The operation of turbine engines at up to $M_\infty \sim 5.5$ and a combination of air-breathing and rocket propulsions as accomplished in SABRE have the potential to lead to a revolutionary change in the mode of propulsion for space transportation. Only by revolutionary changes in modes of propulsion has progress in transportation been made [25,42,43].

SABRE engines on the first stage of a TSTO system allows staging of the second stage at a significantly higher velocity than that feasible with only air-breathing propulsion engines on the first stage. That advantage reduces the size and weight of the second stage. Also, staging at approximately 7.16 km/s could allow the first stage to go around the world and return to the launch site [44].

A viable LEO transportation vehicle or system manifests the following figures of merit [42]: affordability and reliability for exploration, security, and commerce; safety for humans and critical cargo; operational responsiveness for security and emergency human spaceflights; and sustainability for human exploration. The design of this entity is based on the following factors: reference mission, vehicle or system configuration, propulsion, materials and structures, flight controls, operational concept, environment impact, the degree of reusability, integrated health management, and operational and maintenance infrastructures. A revolutionary propulsion system, a high degree of reusability, aircraftlike operations, mature design, and airline industry practices significantly reduce the Earth to LEO transportation cost, a necessary condition to increase demand for civil and commercial use of launch vehicles. Greatly reduced costs lead to commercialization of LEO.

The safety of humans is paramount to entrepreneurs and governments alike. In addition to safe routine journey to and from LEO, the space rescue vehicle to return able and disabled personnel from LEO to Earth is key for safety. It should have a large enough cross range to provide a wide enough daily launch window and range of flight paths to reach a target airfield or alternative landing sites. A rescue vehicle exhibiting a high maximum hypersonic lift-to-drag ratio, preferably ~ 3.5 , could meet that requirement. The space ambulance must also restrict g forces to what is acceptable to disabled humans during entry and descent. For example, the deceleration would be limited to 1.1 g deceleration if a human has a cardiovascular problem.

Can the Skylon concept lead to a viable transport to LEO? The motivation here is to partially address that question with an independent assessment. We address two aspects of this assessment with a level of physics fidelity higher than that feasible with engineering methods.

Our objectives are 1) to determine with CFD the Skylon airframe aerodynamics during powered flight and to compare these results with those developed by reaction engines limited (REL) with engineering methods for the Skylon design, and 2) to assess the impact of SABRE plumes. The aft fuselage is most likely to be engulfed by the plumes at moderate and high Mach numbers because the SABRE engines are mounted on the wing tips, with about one-third of the Skylon fuselage downstream of these engines (Fig. 2). Potential adverse effects of plumes are identified. The value-added assessment presented here includes issues and associated potential design risks not addressed with engineering methods and how to address them. Previous investigations did not address these objectives [45–50].

II. Analysis Approach

Reaction Engines Limited provided CAD data defining Skylon configuration D1.5a, relevant design data at flight conditions of interest, and the corresponding aerodynamic data to compare with those determined in the present study. A CFD analysis was conducted at the provided flight conditions. The fluid is considered inviscid and

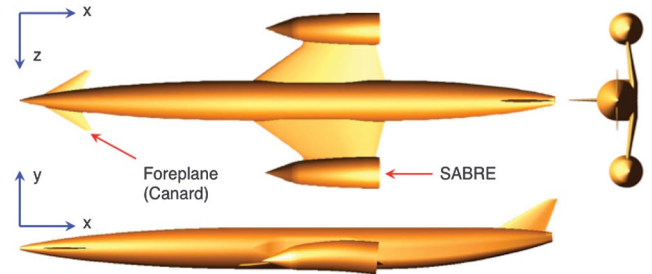


Fig. 2 Skylon D1.5a with inlets closed.

nonradiative. Simulations are performed using the Cart3D package developed at NASA Ames Research Center. The credibility of the simulations is established through computational mesh refinement. Although air is used as the propulsive simulant fluid, care is taken to match nozzle exit pressure, thrust, Mach number, and the ratio of specific heats, γ .

A. Cart3D Simulation Method

The Cart3D simulation package uses a Cartesian cut-cell approach [51,52] in which the Euler equations for inviscid perfect-gas flow are discretized on a multilevel Cartesian mesh with embedded boundaries. The mesh consists of regular Cartesian hexahedra everywhere, except for a layer of body-intersecting cells. The spatial discretization uses a second-order accurate finite volume method with a weak imposition of boundary conditions. The upwind flux-vector splitting approach of van Leer is used [53]. Although the mesh consists of nested Cartesian cells, it is viewed as an unstructured collection of control volumes, making the approach well suited for solution-adaptive mesh refinement. Steady-state flow solutions are obtained using a five-stage Runge–Kutta scheme with local time stepping and multigriding. Domain decomposition via space-filling curves permits parallel computation. Further details are available in [52,54–57]. Freestream air properties are based on the 1976 U.S. Standard Atmosphere [58].

Adjoint error estimates are used to drive mesh adaptation to control and minimize discretization error in the computed simulations through local grid refinement. This procedure is based on an earlier approach for the formulation of reliable local error estimates [59] and the approach for incremental refinement of nested Cartesian cut-cell meshes [60]. The level of discretization error in engineering objectives, typically integral outputs such as coefficients of lift and drag, is reliably and accurately predicted in an affordable and fully automatic manner [57,61], avoiding manual distribution of cells based on “best practices.” This approach not only estimates error in output due to discretization but also provides a cellwise error indicator to guide mesh refinement.

In the simulations described here, a combination of airframe lift and drag coefficients is used as the adaptation functional, and the desired error tolerance is specified. Once the local contributions to errors in these outputs are known, this information guides adaptive cell refinement to reduce the error to below a specified tolerance. Cells introducing large uncertainties are refined to minimize functional error. The flow simulation is then recomputed on the adapted mesh. Several adaptation cycles later, a grid-converged simulation is obtained on a mesh specifically tailored to each flight condition. An important feature of the method is that each simulation is automatically accompanied by convergence histories of both aerodynamic forces and adjoint error estimates as a function of mesh refinement, establishing the credibility of computed forces.

B. Propulsive Boundary Conditions

The SABRE inlet provides air to both the turbine and ramjet engines. This inlet is closed during rocket engine operation. Both the turbine and rocket engines use the same nozzle to expel the combustor chamber fluid. Nozzle profiles similar to those of the Space Shuttle Main Engine are assumed. Nozzles are not gimbaled. The flow coming out from the ramjet engine in the bypass duct

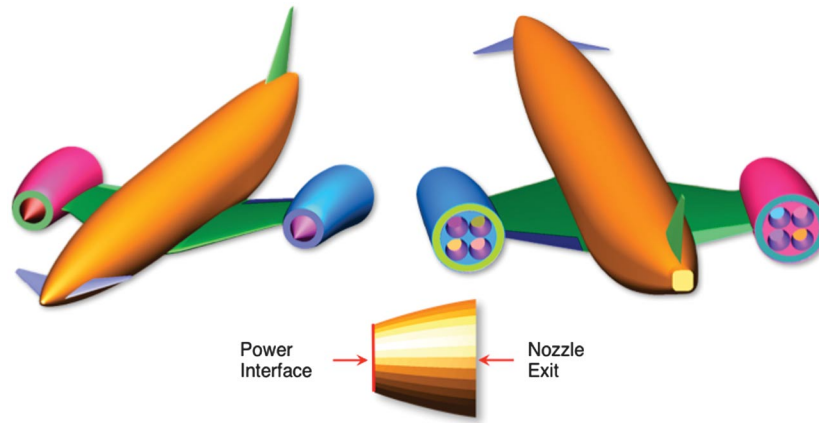


Fig. 3 SABRE 4/Ames engine in turboramjet mode and the nozzle power interface.

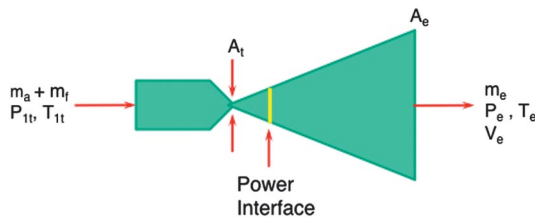


Fig. 4 Air rocket analysis.

(Fig. 1) is accounted for separately. The fluid flow exiting SABRE 4 is modeled to provide the computational boundary conditions.

When either the turbine or rocket engine is in operation, propulsive boundary conditions are applied downstream of nozzle throat but upstream of nozzle exit at the power interface in Fig. 3. The nacelle plume simulation is much more realistic when the propulsive boundary conditions are placed near the nozzle throat than when they are placed at the nozzle exit. When the rocket mode is on, the slip-flow boundary condition is applied along the exit face of the bypass duct.

Because the fluid passing through the nozzle exit is not a perfect gas, the flow conditions at the nozzle exit are converted to those corresponding to cold air (perfect gas) using the exit dynamic pressure ratio $(\gamma_j M_j^2)_{\text{real}} / (\gamma_j M_j^2)_{\text{perfect}}$, where γ is the ratio of specific heats. That is, the exit Mach number is adjusted to correspond to that for cold air γ , while maintaining the “perfect” dynamic pressure that is the same as the “real” nozzle exhaust dynamic pressure. The engine thrust with cold air is essentially[†] [62] the same as that with real exhaust. This scaling also approximately maintains, in cold air simulations, the size and shape of the plume and the distance and location of plume penetration in the freestream fluid [63,64].

The relevant flow conditions at the nozzle power interface are determined in two steps.

1) Flow conditions are calculated at the nozzle exit by solving quasi-one-dimensional mass, momentum, and energy equations from the nozzle throat to the nozzle exit. The nozzle throat and exit areas, combustor chamber pressure, and fuel and oxidizer flow rates are used. Mole fractions are frozen at their values at the throat. Velocity, pressure, density, Mach number, γ_j , gross thrust, and specific impulse are determined at the nozzle exit.

2) Using the real values of γ_j and M_j , the nozzle exit Mach number for $(\gamma_j)_{\text{perfect}} = 1.4$ is determined. Subsequently, flow conditions are obtained at the power interface (Figs. 3 and 4) using isentropic flow relations. These conditions are used as the power interface boundary conditions.

[†]We use the word “essentially” because one-dimensional analysis is conducted to determine cold air conditions at the nozzle exit and because, in real exhaust, chemical reactions are still taking place, which are not accounted for in computing the cold-air thrust [62].

During the rocket mode of operation of SABRE 4, steps 1 and 2 lead to the gross thrust that is 104.2% of the value that REL provided. These thrust values are based on one-dimensional analyses. The computed gross thrust values from three-dimensional simulations are 105% of the REL value. Please note that the technical specification lists gross thrust to be approximately 2 MN per nacelle in the Mach number range from 5.2 to 27.8 ([36] p. 6).

In the case of turboramjet operation, the assumption is made that the combustion chamber is directly connected to the nozzle. An air-rocket analysis is conducted (Fig. 4). The fuel flow rate m_f , airflow rate m_a , total pressure P_{1t} , and total temperature T_{1t} are known at the exit of the combustion chamber. From these quantities, thermoequilibrium total enthalpy and total entropy are obtained. The nozzle throat conditions are determined assuming an isentropic process to the throat pressure from the combustor chamber exit, such that the Mach number at throat is unity. The throat area A_t and exit area A_e are also known. (The former is different from that for the rocket engine, and the latter is the same as that for the rocket engine.) Subsequently, the aforementioned step 1 is applied up to the power interface, and the isentropic process is used to obtain nozzle exit conditions. (If step 1 were followed all the way to the nozzle exit, the thrust per nozzle would have been 107.1% of the value obtained when the isentropic process is used from power face to the exit.) Step 2 is then followed.

The performance of the ramjet engine, the design of the bypass duct (Fig. 1), and the engine design at the exhaust plane were unavailable for SABRE 4 because the latter was yet to be developed. The CAD files we received from REL did not provide any information about the placement of nozzles and the bypass on the nacelle exit plane. We had only the total nacelle exit area and the exit area of each nozzle for the scaled SABRE 3. There was a mismatch between the CAD geometry and the propulsion design parameters we were provided.

The one-dimensional ramjet engine exit boundary conditions for the scaled SABRE 3 are assumed for the SABRE 4/Ames engine and applied at the exit face of the bypass duct. The key difference between the SABRE 4 and SABRE 4/Ames engines is that the bypass duct exit area of the latter engine is 70.6% of that of the former engine. Because of the treatment of the turbine engine as an air-rocket engine and the use of a smaller duct area, the gross thrust of the SABRE 4/Ames engine is 87.5% of the scaled SABRE 3 engine. In the Mach number range from 0 to 5.5, the technical specification lists approximate gross thrust to be 0.8 to 2 MN per nacelle ([36] p. 6). Note that the assumption made at the bypass duct boundary has no consequence on airframe aerodynamic forces, the focus of this study. The nacelle plume shape could be somewhat different, but that is of negligible consequence at $M_\infty = 3.508$, the air-breathing powered flight condition studied.

C. Engineering Method

Reaction Engines Limited provided the following information regarding the engineering method they used. They performed trajectory and design analyses on Skylon with a computer program

incorporating methods for calculating the lift and drag coefficients on slender-bodied winged vehicles. Calculated values were compared with experimental data for a delta-wing aircraft configuration (RM A57K14) and the RM-10 experimental missile to validate these methods. The error in calculated value was typically around 10%.

Aerodynamic lift is modeled as the sum of linear forebody and wing lift plus a nonlinear hypersonic term dependent on vehicle plan area. Forebody lift is calculated by applying linearized potential flow theory. Wing lift is computed from delta wing flow theory assuming that the gross wing area is effective (that is, including the wing planform embedded in the fuselage except for the triangular portion ahead of the wing leading-edge/fuselage intersection, which is included in the forebody). Similarly, the wing tips are assumed to extend to the nacelle centerlines to approximately model the external aerodynamic lift on the nacelles.

The Mach number range is split into three regimes: subsonic (M_∞ from 0 to 1), transonic (from $M_\infty = 1$ to the supersonic leading-edge Mach number M_{LE}), and supersonic ($M_\infty > M_{LE}$). Subsonic lift is composed of a linear potential flow term plus a nonlinear vortex flow term. The transonic regime is correlated by the transonic similarity parameter and modeled by a curve fit to theoretical and experimental data. At the supersonic leading-edge Mach numbers, the lift curve slope collapses onto a single curve independent of aspect ratio. At hypersonic Mach numbers, a nonlinear lift component becomes progressively important and is represented by a Newtonian flow model.

Vehicle drag is modeled as the sum of wave, base, and induced friction drag terms of the individual vehicle components. The vehicle forward and aft fuselage are specified by a Sears-Haack profile, which gives minimum wave drag for a given length and volume. The center fuselage section (corresponding to the wing root chord) is cylindrical to reduce the overall vehicle cross section in the region of the wings/nacelles. Further area ruling is achieved by narrowing the fuselage sides in the payload bay region; however, the effect this has on the drag has not been assessed. Wing wave drag is assumed to rise linearly from Mach 0.9 to a constant transonic value. Above the supersonic leading-edge Mach number, the wave drag decays until at hypersonic Mach numbers, when second-order terms become significant. Fuselage base drag is modeled by curve fits to experimentally derived data of base pressure coefficient versus Mach number for streamline bodies.

The suction surface flow detaches at subsonic speeds, and the leading-edge suction is approximately zero due to the wing sharp leading edge. And the normal force vector acts at right angles to the vehicle centerline because the forebody and wing have zero camber. Therefore, induced drag can be estimated by assuming that the vehicle behaves as a flat plate throughout the Mach number range. This induced drag model is likely to be mildly pessimistic in the subsonic regime. Skin friction is evaluated by calculating a skin friction coefficient corresponding to the appropriate length-based Reynold's number and a reference temperature to allow for kinetic heating.

D. Simulation Credibility

The objective is to obtain aerodynamic forces such that they are independent of the computational mesh. The verification of derived aerodynamic forces for every flight condition is conducted with adjoint-based mesh adaptation using an integrated force objective function, $J = C_L + C_D$. Three examples of adaptation are presented: 1) $M_\infty = 5.0$ unpowered flight at $\alpha_v = \alpha_f = 10$ deg with inlet closed, 2) $M_\infty = 3.508$ powered flight at $\alpha_v = 4.521$ deg, $\alpha_f = -0.294$ deg, and 3) $M_\infty = 12.189$ rocket-powered flight at $\alpha_v = \alpha_f = 7.512$ deg. Herein, α_v and α_f are, respectively, vehicle angle of attack and foreplane (canard) angle of attack.

Figure 5 presents for example 1 the convergence of the aerodynamic forces and moment, the functional, and the remaining error estimates. Excellent mesh convergence for the integrated forces and flowfield is observed. There are virtually no changes in forces and moment over the last two adjoint-driven adaptations (Fig. 5a). Figure 5b shows the value of the functional J on each mesh adaptation. Adjoint error estimates are very well behaved. At the last adaptation, 22 million cells are used.

A very high resolution of the flowfield is achieved with mesh adaptation. Figure 6 presents the cell distribution near Skylon and the pressure isobars on its surface in a horizontal plane, vertical plane, and cross plane on the top, middle, and bottom of this figure, respectively. Regions with high-pressure gradients are observed. The cell density is high in regions where rapid changes in flow properties occur over short distances, affecting aerodynamic forces. For example, the simulation of the inlet cone shocks and the nacelle-wing corner shocks require a high concentration of cells (Fig. 6, bottom). Because the adaptation uses a threshold level, invariably there are slight asymmetries in the adapted mesh (Fig. 6, bottom left). Despite these asymmetries, the discrete simulation displays almost perfect symmetry about the vehicle centerline (Fig. 6, bottom right). Figure 7 presents isobars on the top and lower surfaces of Skylon, showing complex shock-shock interactions.

Figure 8 presents for case 2 the convergence of the aerodynamic forces, the magnitude of update to the functional, and the adjoint estimate of error. Over the last two adjoint-driven adaptations, there is virtually no change in the drag coefficient, and the lift coefficient has almost achieved its asymptotic value (Fig. 8a). At the last adaptation, 26 million cells are used. Figure 8b shows that the estimate of error and the magnitude of update to the function are in the asymptotic range. Figure 9 shows the cell distribution in the symmetry plane.

Figure 10 shows the history of the force coefficients as the number of cells is increased for a rocket-powered flight at $M_\infty = 12.189$. The force coefficients nearly achieve their asymptotic values when there are 8 million cells. That observation is also valid for cases 1 and 2. Also Fig. 10 shows the convergence of the adjoint estimate of error bound and the update to the functional as functions of the number of cells. Figure 11 shows the cell distribution and pressure field in the symmetry plane and the surface pressure field.

The cell distributions for cases 1, 2, and 3 differ in Figs. 6, 9, and 11, respectively, because freestream conditions and engine operations are different. The simulation method used here automatically tailors

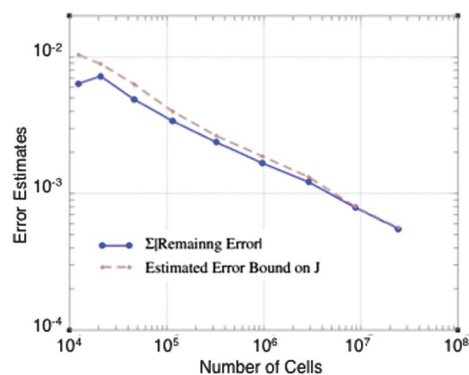
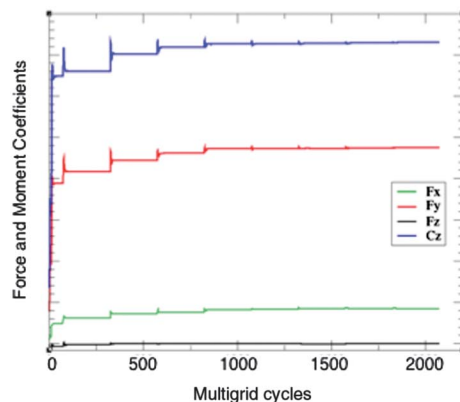


Fig. 5 Mesh convergence at $M_\infty = 5.0$ and $\alpha = 10$ deg with engine inlets closed.

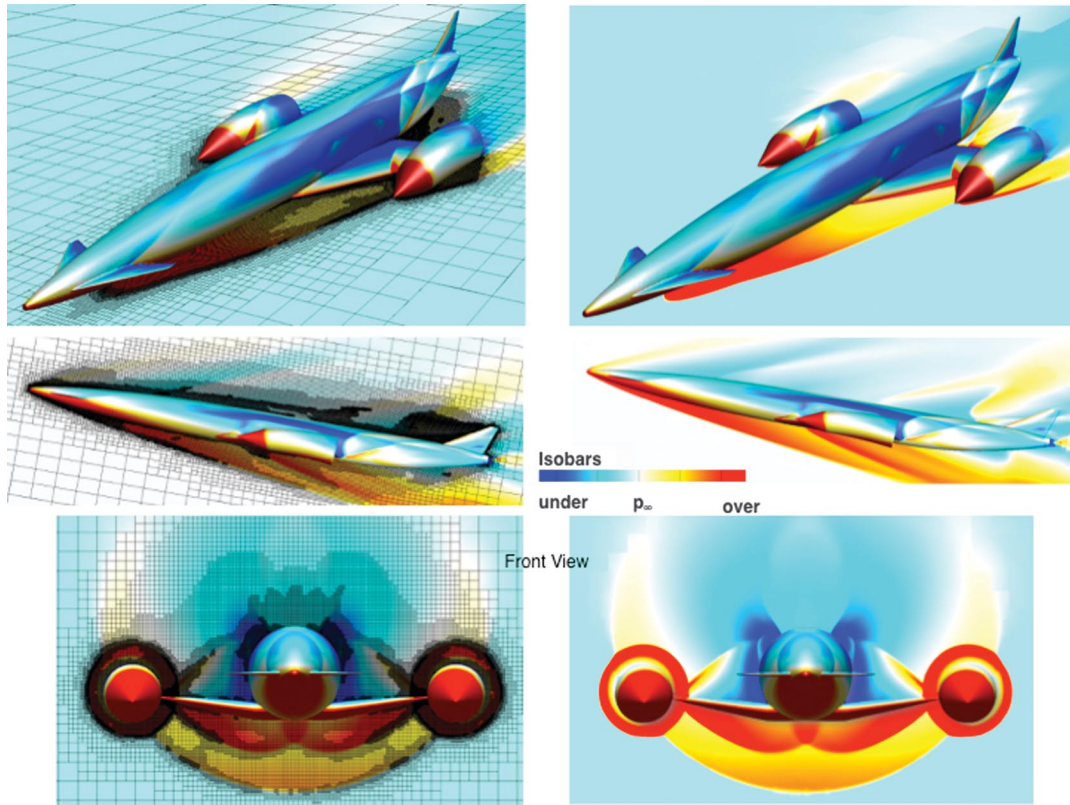


Fig. 6 Isobars on the surface and in different planes with cells at $M_\infty = 5.0$ and $\alpha = 10$ deg for unpowered flight with inlets closed.

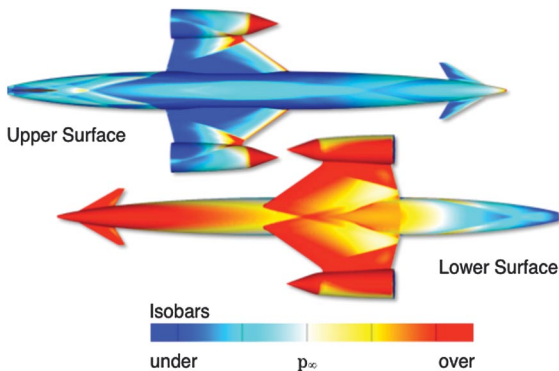
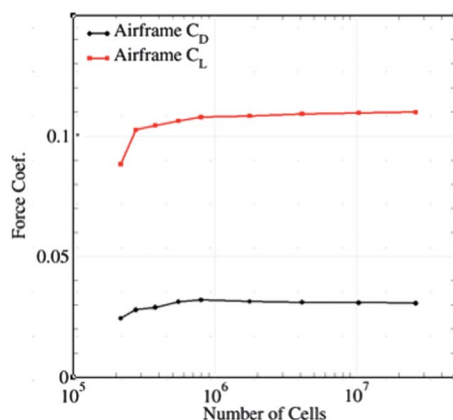


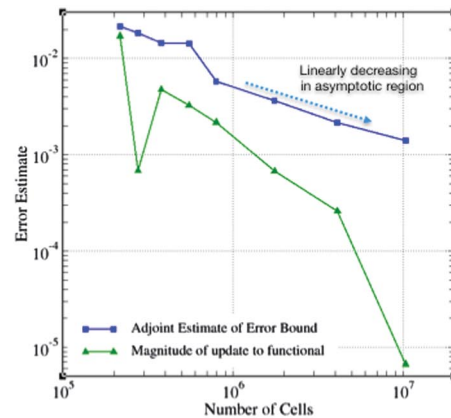
Fig. 7 Isobars at $M_\infty = 5.0$ and $\alpha = 10$ deg for unpowered flight with inlets closed.

the mesh to flow conditions such that the desired level of credibility in the force coefficient is achieved.

In the absence of wind-tunnel test data for Skylon, some circumstantial evidence of the validity of simulated Cart3D forces is provided. A liquid glideback booster having canards similar to the Skylon foreplanes was tested at $M_\infty = 3.0$ [65]. Figure 12 compares lift and drag coefficients derived from the Cart3D simulations with both wind-tunnel data and Reynolds-averaged Navier–Stokes simulations determined using the NASA Overset Grid Flow (OVERFLOW) code, version 1.8t [66]. Agreement is excellent over a range of incidence angles from -5 to $+30$ deg. At these conditions, friction drag is roughly two orders of magnitude lower than profile and wave drag. Close inspection of Cart3D predictions shows a very slight deficit in drag because the simulations are inviscid. This discrepancy is, at most, only 1–2% and is negligible compared with other modeling uncertainties.



a) Convergence of forces with adaptation



b) Convergence of error bound

Fig. 8 Mesh convergence for turboramjet-powered flight at $M_\infty = 3.508$, $\alpha_v = 4.521$ deg, and $\alpha_f = -0.294$ deg.

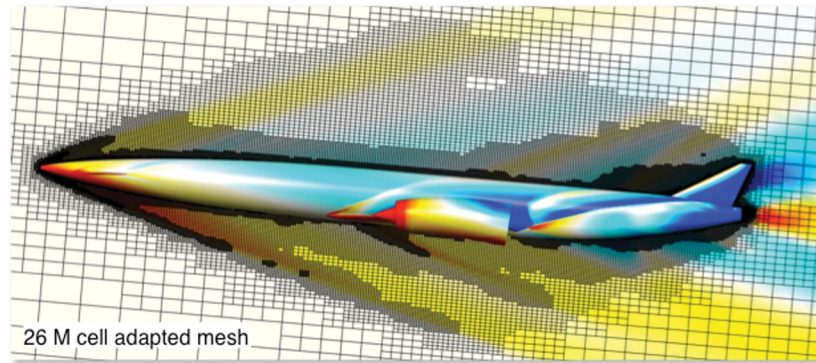


Fig. 9 Cells in the symmetry plane and isobars for turboramjet-powered flight at $M_\infty = 3.508$, $\alpha_v = 4.521$ deg, and $\alpha_f = -0.294$ deg.

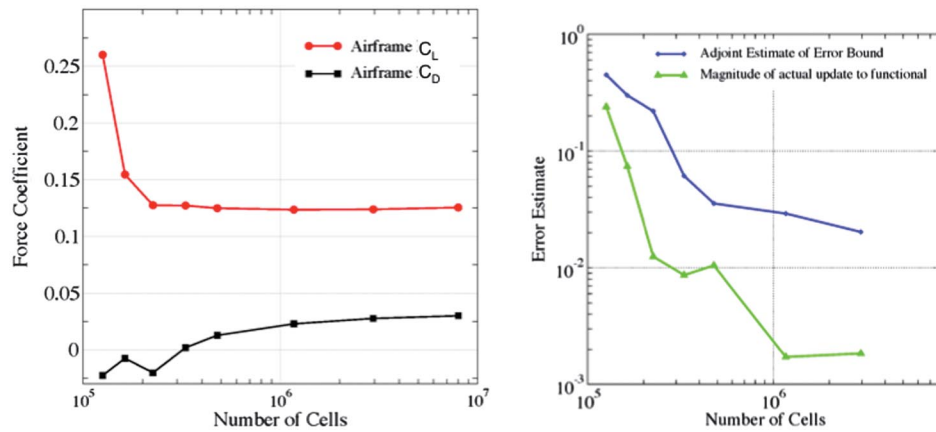


Fig. 10 Mesh convergence for rocket-powered flight at $M_\infty = 12.189$ and $\alpha_v = 7.512$ deg.

III. Airframe Aerodynamics and Thermal Environment

At select flight conditions, the aerodynamics of Skylon D1.5a is assessed when the engine is operated in turboramjet and rocket modes. Aerodynamic data produced by REL's engineering methods are checked against those derived from Cart3D simulations at flight conditions listed in Table 1.

The Mach fields in a horizontal plane as observed from the top of an unpowered Skylon are presented in Fig. 13a for case 1 in Table 1 and in Fig. 13b for case 2 with the engine inlet closed and open (with the inlet cone vertex at 2690 mm upstream of the inlet entrance),

respectively. The shock waves on the wings have a more complex structure, and the flowfield downstream of the nacelles is quite different when the inlets are closed from when they are open. The computed airframe pressure forces for case 2 are compared with those determined using engineering methods by REL in Table 2. The agreement is excellent.

Powered flight simulations were conducted for cases 3–13 (Table 1). At $M_\infty = 3.508$, the SABRE 4/Ames engine is operated in turboramjet mode (case 3). The foreplane is at $\alpha_f = -0.2942$ deg, and the inlet cone is extended upstream of the inlet face by 2900.1 mm. At other Mach numbers, the foreplane is at the same

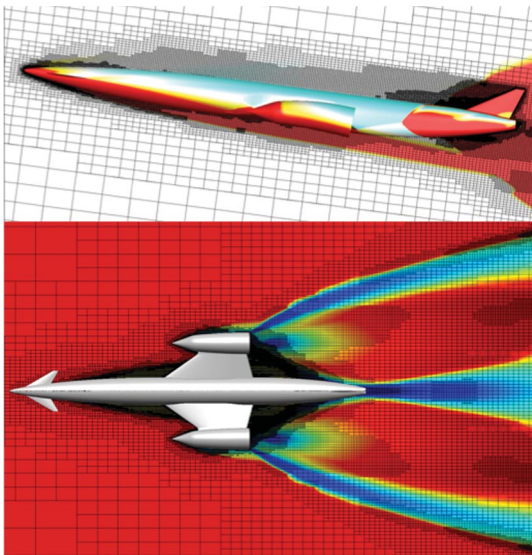


Fig. 11 Cells and isobars in the symmetry plane (top) and top view (bottom) for rocket-powered flight at $M_\infty = 12.189$ and $\alpha_v = 7.512$ deg.

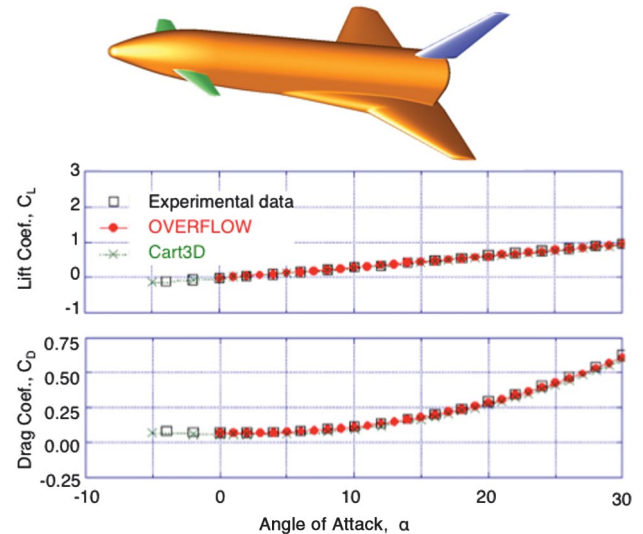


Fig. 12 Comparison of Cart3D simulations with experimental and OVERFLOW simulations at $M_\infty = 3.0$ (bottom) for a glideback booster (top).

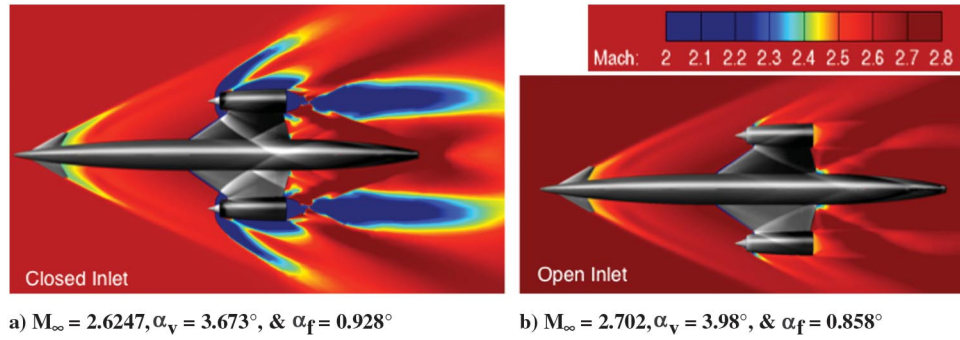


Fig. 13 Mach number contours and shock patterns for unpowered flight.

angle as the vehicle angle of attack, the inlet is closed, and both powered (with SABRE operating in the rocket mode) and unpowered flight simulations are performed.

At $M_\infty = 3.508$, $\alpha_v = 4.521$ deg, and $\alpha_f = -0.294$ deg with the turboramjet operational, Fig. 14 presents nondimensional temperature patterns in nacelle plumes, Mach contours, and cell distributions in different planes. The width of the nacelle plume in the vicinity of Skylon is nearly the same as the width of the aft end of SABRE. The interaction of engine exhaust from four nozzles and from the bypass duct creates a complex flowfield. Nacelle plumes do not impact or engulf the Skylon empennage. The inlet cone forms a shock wave that hits the fuselage in a region upstream of the empennage. Figure 15 compares pressure forces derived from Cart3D simulations and those obtained with engineering methods by REL, with C_L comparing very well and C_D not so well. Consequently, the lift/drag ratio is overestimated by the engineering methods. This is due to an accounting inconsistency; we included the nacelle external drag as part of the airframe drag, whereas REL counted it as part of the engine thrust accounting.**

Kaleidoscopic flow patterns are observed in Fig. 16 as the freestream Mach number is increased from 6.673 to 16.969 during the rocket-powered ascent flight, where thermal environments around Skylon are shown as viewed from the top. The SABRE/Skylon wake width increases as rocket plumes are increasingly underexpanded with increasing Mach number and altitude. Static temperatures in the gas next to the wing increase as the freestream Mach number and altitude increase and the dynamic pressure decreases. Also, the plume–freestream interaction regions are hotter than the core region of the plume downstream of Skylon at higher Mach numbers.

A remarkable change in nacelle plume geometry via isostagnation enthalpy contours is observed in Fig. 17, when the freestream Mach number is increased from $M_\infty = 6.673$ to 12.189. At $M_\infty = 12.189$ and an altitude of 65.16 km, the nacelle plumes engulf the Skylon aft fuselage. The normalized temperatures at $M_\infty = 12.189$ are significantly higher than those observed at $M_\infty = 3.508$ (Figs. 14 and 17b).

Figure 18 presents perspective views of the thermal environment around the aft fuselage and in a plane downstream of a Skylon nacelle. At $M_\infty \geq 12.189$, there are regions where the static temperature is roughly 8–16 times that of the freestream temperature. Where the SABRE plume shock wave hits the fuselage, there is a static temperature spike. Subsequently, the static temperature again increases as hot gases from engines pass over the aft fuselage (Figs. 18c and 18d). As seen in Fig. 19, two plume shock waves, one from each SABRE, intersect at the vehicle symmetry plane. In front of the vertical tail, there is a bow shock wave. This shock wave also elevates static temperatures on the fuselage around the base of the vertical tail.

At $M_\infty = 16.969$, approximately 20% of the aft portion of the fuselage, including the empennage, is surrounded by fluid at very high static temperatures. As the rocket mode is used to beyond

$M_\infty = 17$, the percentage of fuselage engulfed with nacelle plumes will further increase, and the thermal environment will become increasingly severe. The thermal environment will also depend on how the SABRE nozzles are gimballed. However, the plumes are so underexpanded that it is unlikely this will substantially alleviate the impingement effects.

At $M_\infty = 12.189$, for a perfect gas with $\gamma = 1.4$, the freestream total temperature is approximately 30 times $T_\infty = 231$ K, and the freestream recovery temperature is roughly 26 times T_∞ . However, based on real gas chemistry, for the case where surface pressure equals atmospheric pressure, the freestream total and recovery temperatures are only about 13 and 11 times the freestream temperature (as shown in Table 3), respectively, for an assumed recovery factor of 0.85.

Table 1 Simulated flight conditions

Case	Mach number M_∞	Altitude, km	Vehicle α_v , deg	Foreplane α_f , deg	Dynamic pressure, Pa	Engine mode
1	2.625	15.326	3.673	0.928	55,486	Inlet closed; none
2	2.702	15.833	3.980	0.858	53,985	Inlet open; none
3	3.508	18.537	4.521	−0.294	59,412	Turboramjet
4	5.188	28.084	6.577	6.577	30,055	Rocket or none
5	5.490	30.392	7.693	7.693	23,815	Rocket or none
6	5.936	33.852	9.324	9.324	16,713	Rocket or none
7	6.673	39.695	11.583	11.583	9,322	Rocket or none
8	7.483	45.722	12.779	12.779	5,330	Rocket or none
9	8.577	51.983	12.453	12.453	3,210	Rocket or none
10	10.131	58.483	10.626	10.626	1,965	Rocket or none
11	12.189	65.160	7.512	7.512	1,163	Rocket or none
12	14.952	71.854	3.510	3.510	648	Rocket or none
13	16.969	75.771	0.907	0.907	440	Rocket or none

Table 2 Airframe pressure forces with flow through unpowered engine for Case 2, Table 1

Airframe force	Cart3D	REL
Lift C_L	0.129	0.127
Drag C_D	0.0287	0.0291
C_L/C_D	4.495	4.364

**In rocket mode, REL accounts the nacelle external drag as part of the airframe drag.

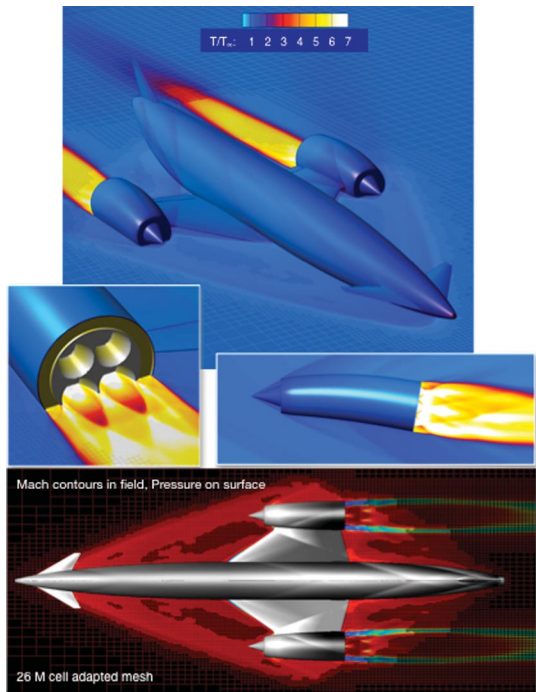


Fig. 14 Plume static temperature, Mach contours, surface pressure, and mesh for turboramjet-powered flight at $M_\infty = 3.508$, $\alpha_v = 4.521$ deg, and $\alpha_f = -0.294$ deg.

Because Cart3D simulated temperatures are based on Euler equations for a perfect gas, which account for neither frictional heating nor radiative cooling on the surface, they do not translate directly into Skylon skin temperatures. The surface radiation-equilibrium thermal environment will differ when simulations are conducted with air and hydrogen/oxygen chemistry and account for viscous (i.e., frictional heating), plume radiation, and real gas effects. This increased level of physics will provide information such as surface temperatures, flow separation, and realistic effects of shock–shock and shock–surface interactions.

High-temperature gas will emit significant radiation in the UV, visible, and infrared regions of the electromagnetic spectrum, leading to potentially substantial heating of aft fuselage surfaces. Radiative processes augment convective heating. At the expected temperatures, an estimated radiative heating of the body surfaces can be reasonably obtained using a gray-gas model. Should the estimated radiative heating turn out to be a significant fraction of the convective heating, a compositional distribution, in terms of gas species populations, would be necessary to conduct a full-line radiation analysis to perform an accurate radiation heating assessment [67].

Two of the key problems with the HOTOL design were the far aft location of the center of gravity and poor control authority with far aft wings. The solutions to these problems dictated the locations of the SABRE engines and wings on the Skylon concept. If aft fuselage heating and vibroacoustic loads at $M_\infty > 8.5$ are issues that cannot be addressed with appropriate structures and materials, then the overall design of Skylon D1.5a must be changed without reintroducing these HOTOL problems.

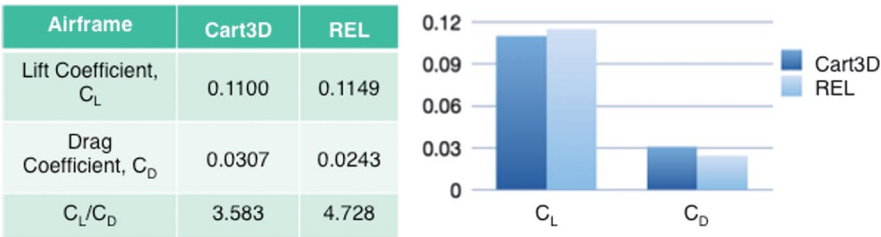


Fig. 15 Cart3D and REL pressure forces at $M_\infty = 3.508$, $\alpha_v = 4.521$ deg, and $\alpha_f = -0.294$ deg.

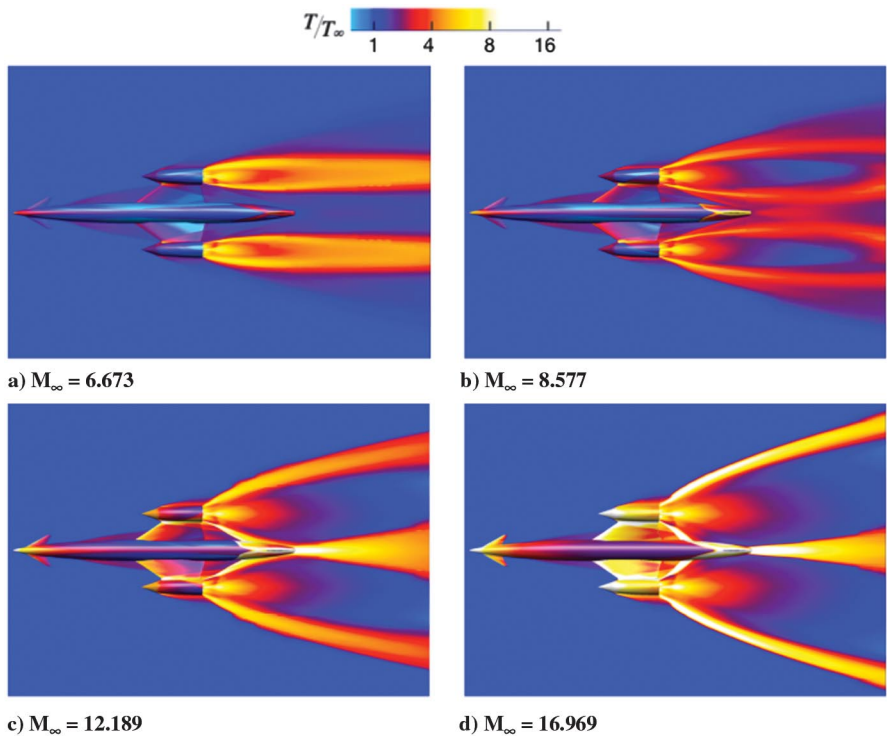


Fig. 16 Thermal environments, as viewed from the top.

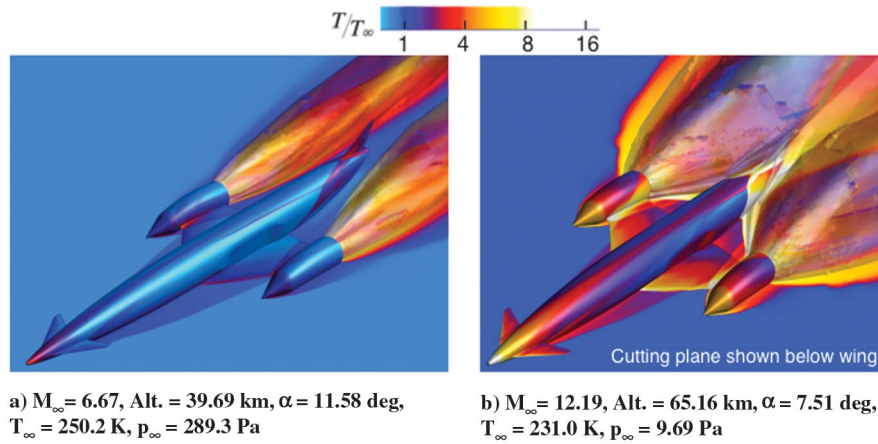


Fig. 17 Thermal environments and nacelle plume geometries via isostagnation enthalpy contours and temperature ratios.

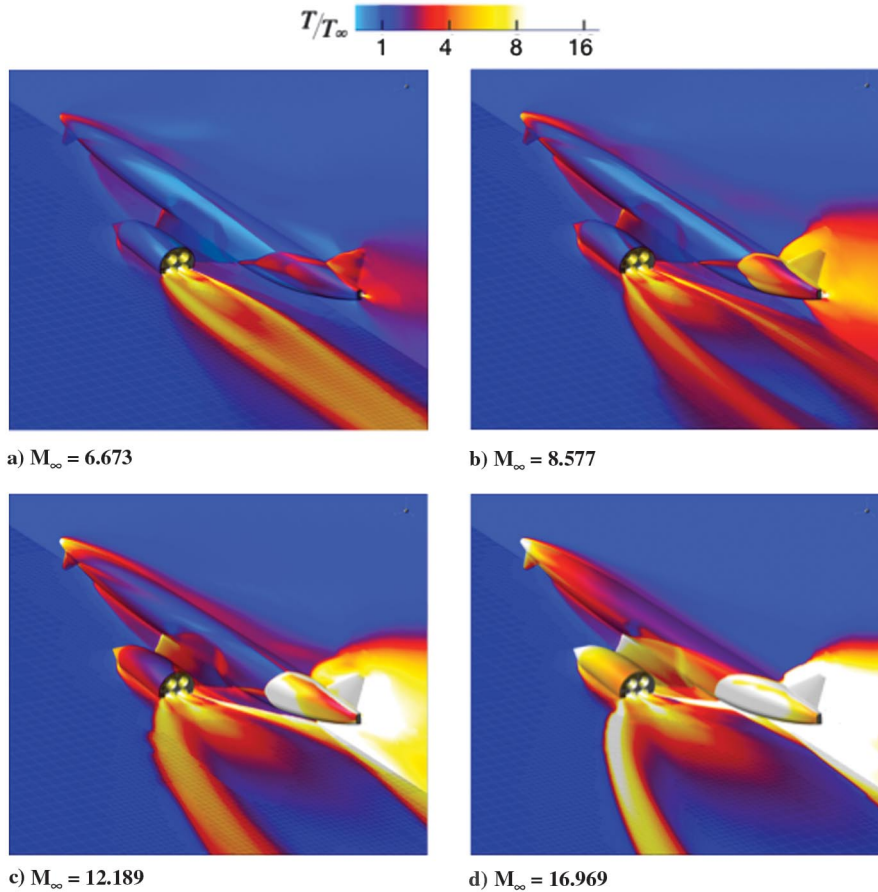


Fig. 18 Thermal environments around Skylon and in a plane through the center of lower two SABRE nozzles.

Figure 20 presents the pressure field around Skylon as viewed from the top, at different Mach numbers. As the Mach number and spaceplane altitude increase and dynamic pressure decreases, relative pressure near the aft end of the Skylon fuselage increases, which in turn favorably affects the airframe force coefficients by both increasing C_L and reducing C_D .

Figure 21 compares pressure lift and drag coefficients as determined by Cart3D simulations (with and without rocket power) and those determined with engineering methods by REL. These coefficients increase and decrease with the increase and decrease in the angle of attack, respectively. The Cart3D lift coefficients for the poweroff conditions compare extremely well with those REL provided, except at $M_\infty \sim 17$. The comparison of drag coefficients is less satisfactory but still in fair agreement. This verdict could be due to the inclusion of friction drag and the assumptions made in the

engineering method vis-à-vis the Cart3D approach. The key differences in airframe C_L ($C_{L_{\text{powered}}} - C_{L_{\text{thrust}}}$) and C_D ($C_{D_{\text{powered}}} - C_{D_{\text{thrust}}}$), as derived from Cart3D simulations and REL data, are for powered flight at $M_\infty > 8.5$ when nacelle plumes begin to engulf the aft fuselage. The impact of plumes on airframe aerodynamics is not accounted for in REL's method of computing

Table 3 Freestream total and recovery temperatures for a real gas

M_∞	Altitude, ft	p_∞ , psi	T_∞ , °R	T_{tot} , °R	T_{tot}/T_∞	T_{rec} , °R	T_{rec}/T_∞
10.13	190,285	0.004166	445.0	4588.0	10.31	4400.0	9.89
12.19	213,252	0.001583	419.9	5367.0	12.78	4632.6	11.03
14.95	235,561	0.000573	387.4	6735.8	17.39	6282.6	16.22
16.97	248,685	0.000304	372.0	6971.2	18.74	6717.0	18.06

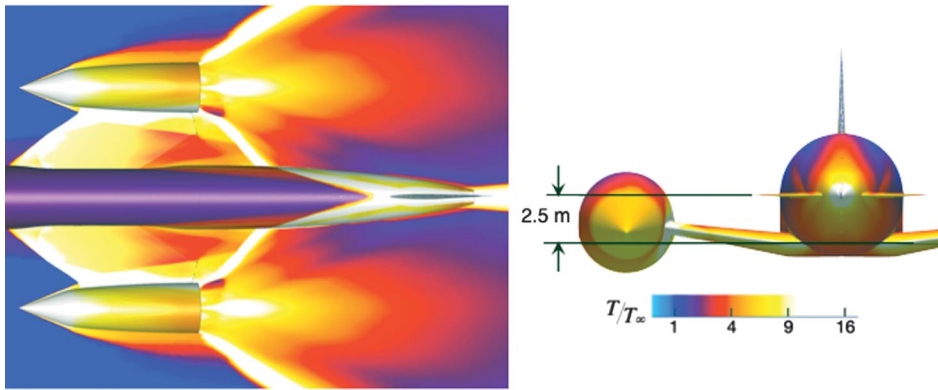


Fig. 19 Thermal environment around the aft fuselage and in a cutting plane at $y = -2.5$ m of Skylon at $M_\infty = 16.969$.

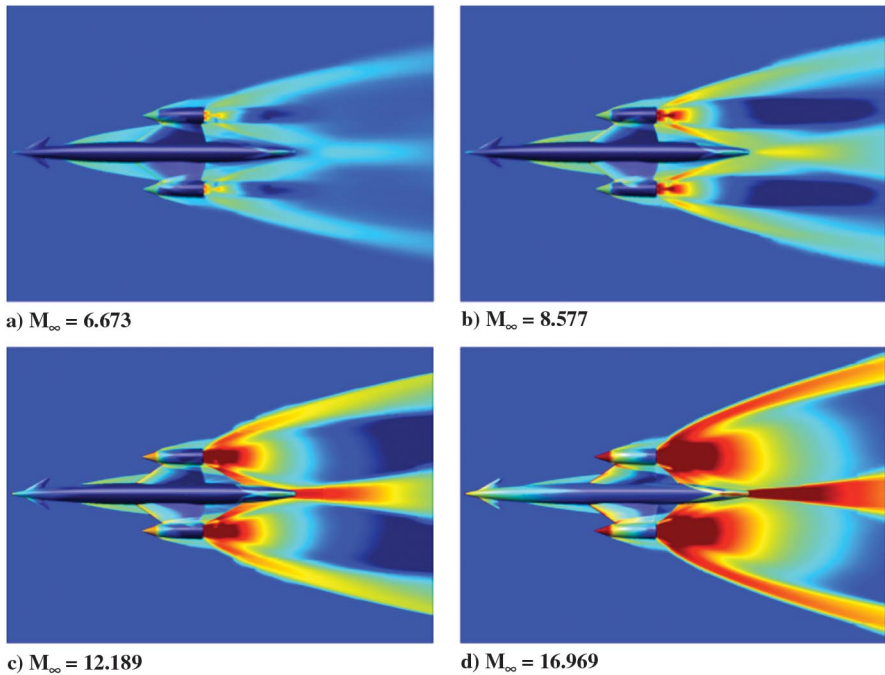


Fig. 20 Pressure fields as viewed from the top.

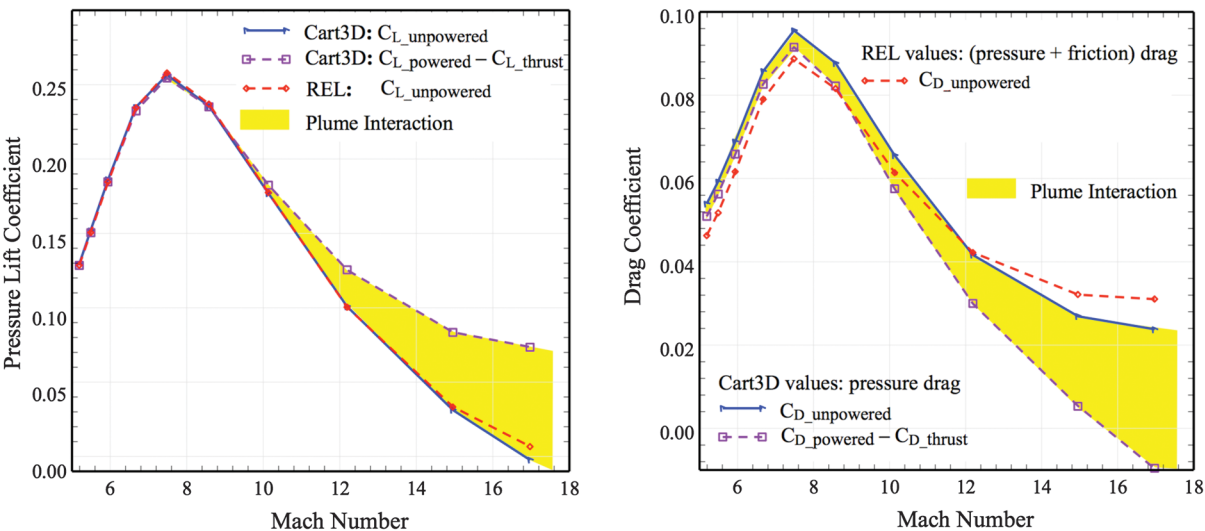


Fig. 21 Effects of jet interactions on pressure forces.

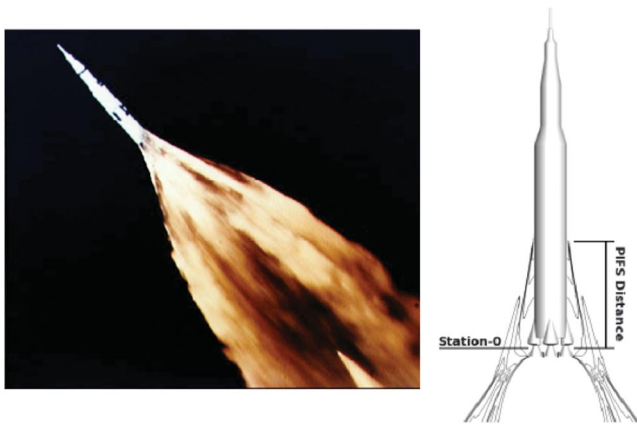


Fig. 22 PIFS on Apollo 11.

forces. The effects of this shortcoming increase with M_∞ beyond 8.5, as illustrated by the yellow region that depicts the plume interaction increments for C_L and C_D .

Another potential adverse impact of nacelle plumes is the effect of plume-induced flow separation (PIFS) on nacelles and on the fuselage only where plume shocks impinge. On Apollo 11, PIFS distances were 15 and 33 m, respectively, at $M_\infty = 4.4$ and $p_\infty = 151$ Pa, and at $M_\infty = 6.5$ and $p_\infty = 22$ Pa (Fig. 22 [68]). The PIFS effect can only be determined with viscous simulations. This effect will increase the portion of airframe (aft fuselage, wings, and nacelle) that is engulfed by SABRE plumes. The thermal environment of the engulfed portions of Skylon will have an adverse effect on structures and materials. The PIFS effect also will affect the airframe aerodynamics. Additionally, shock waves interacting with boundary layers may cause flow separation. If plumes and shock waves adversely affect performance, mission, cost goals, or reusability, some adjustments in design, mission, flight profile, or propulsive power will be required.

IV. Conclusions

A revolutionary propulsion breakthrough is possible with the REL heat exchanger technology, which could lead to dramatic improvements in the transportation of medium-weight payloads to LEO in terms of affordability, reliability, safety, resiliency, and operational responsiveness. It might also make hypersonic transportation a reality. This technology was used to develop a conceptual design of the SABRE engine. The conceptual Skylon aerospace plane is powered with this innovative and potentially game-changing air-breathing rocket combined-cycle engine.

Can the Skylon concept lead to a viable transport to LEO? The motivation here was to partially address that question. Two aspects of this assessment were addressed with a higher level of physics fidelity than is possible with engineering methods. Both the Skylon airframe aerodynamics during powered flight and the impact of engine plumes on the aft fuselage were studied to provide a value-added independent assessment.

At all flight conditions considered, CFD simulations were performed with the Cart3D package. The fluid is considered to be inviscid perfect gas with no radiation. Although air is used as the simulant fluid, care was taken to match both exit-engine pressure and thrust to those produced by the SABRE nozzles. The credibility of the simulations was established with computational mesh refinement. The final forces derived from the simulations are essentially independent of the computational mesh.

The adverse thermal impact of an underexpanded plume on the aft fuselage increases as M_∞ increases above 8.5. The simulation at $M_\infty \geq 12.19$ shows that, downstream of the SABRE engines, there are regions where static temperatures are roughly 8–16 times greater than the freestream temperature for the perfect gas model used. From $M_\infty = 10.13$ to 16.97, the freestream total and recovery temperatures (normalized with freestream temperatures), based on

real gas chemistry, atmospheric pressure, and 0.85 for the recovery factor, vary from 10.31 to 18.74 and from 9.89 to 18.06, respectively.

Because simulated thermal environments are based on Euler equations with $\gamma = 1.4$, they do not quantitatively predict the fuselage skin temperatures. Viscous simulations, including air and hydrogen/oxygen chemistry, radiant heating from plumes, proper heat transfer condition at the Skylon surface, and proper γ , are necessary to determine surface temperatures. Viscous simulations are also needed to determine PIFS on the nacelles and the aft fuselage.

If the thermal and vibroacoustic loads induced on the fuselage due to nacelle plumes cannot be accommodated with any structures or materials technology, the overall design of Skylon must be radically modified. Detrimental effects of PIFS, shock-wave-induced boundary-layer separations, and shock–shock interactions might also require some adjustments in design, mission, flight profile, or propulsive power.

Unpowered airframe pressure lift and drag coefficients, determined with Cart3D, generally agree with those that REL computed with engineering methods. The comparisons of lift and drag coefficients are excellent and fair, respectively. During powered flight, the nacelle plume significantly increases fluid overpressure at $M_\infty > 8.5$ in the immediate vicinity of the Skylon aft fuselage. This favorable impact of plumes pressurizes the aft fuselage. Consequently, the airframe lift coefficient increases, and the airframe drag coefficient decreases. The force coefficients based on engineering methods do not account for the impact of plumes and plume shocks on the aft fuselage.

The HOTOL concept evolved into the Skylon concept. The second revival of the Aerospace Plane Program is essential to develop and demonstrate a SABRE-powered experimental aerospace plane (X-plane) before the Skylon concept can be evolved into an operational aerospace plane for viable transport to LEO. The goal for this X-plane should be to achieve a speed of 6.8 to 7.8 km/s. The development of these vehicles necessitates the judicious use of a combination of engineering methods, advanced methods based on required physics or analytical fidelity, test data, and independent assessments, with the focus on the figures of merit mentioned in Sec. I for achieving viability. The development of the proposed X-plane entails visionary leadership and will to achieve a successful flight demonstration. Its execution should be guided by lessons learned from previous aerospace plane programs.

Acknowledgment

Unmeel Mehta is appreciative of Reaction Engines Limited for providing Skylon concept data and describing the engineering method used for lift and drag calculations.

References

- [1] Augenstein, B. W., et al., "The National Aerospace Plane (NASP): Development Issues for the Follow-on Vehicle, Executive Summary," RAND Corp. Rept. R3878/1-AF, Santa Monica, CA, 1993.
- [2] Butrica, A. J., "Reusable Launch Vehicles or Expendable Launch Vehicles? A Perennial Debate," *Critical Issues in the History of Spaceflight*, edited by Dick, S., and Launius, R., NASA SP-4702, 2006.
- [3] Hallion, R. P., and Young, J. O., "Space Shuttle: Fulfillment of a Dream," *The Hypersonic Revolution*, edited by Hallion, R. P., Vol. 2, Dept. of the Air Force, Hqs. Aeronautical Systems Center :AFD-100927-035, Wright-Patterson AFB, OH, 1987, p. 1036.
- [4] Jenkins, D., *Space Shuttle, The History of the National Transportation System*, 3rd ed., 2001, p. 108.
- [5] Heppenheimer, T. A., *The Space Shuttle Decision*, NASA SP-4221, 1999.
- [6] "Report on Why and Whither Hypersonics Research in the US Air Force," U.S. Air Force Scientific Advisory Board TR-00-03, Washington, D.C., Dec. 2000, p. 6.
- [7] Hannigan, R. J., *Spaceflight in the Era of Aero-Space Planes*, Krieger, Malabar, FL, 1994, p. 78.
- [8] "National Aero-Space Plane, Restructuring Future Research and Development Efforts," U.S. General Accounting Office Rept. GAO/NSTAD-93-71, Washington, D.C., Dec. 1992.
- [9] "Report of the Defense Science Board on National Aero-Space Plane (NASP) Program," Defense Science Board AD-A274530, Washington, D.C., Nov. 1992, p. 12.

- [10] "Access to Space Study," NASA TM-109693, Jan. 1994.
- [11] Mehta, U., and Bowles, J., "Two-Stage-to-Orbit Spaceplane Concept with Growth Potential," *Journal of Propulsion and Power*, Vol. 17, No. 6, Nov.-Dec. 2001, pp. 1149-1161.
doi:10.2514/2.5886
- [12] Hunt, J., et al., "Airbreathing Launch Vehicle Study," *Presented at the 50th JANNAF Propulsion Meeting*, Salt Lake City, UT, July 2001.
- [13] Hueter, U., and McClinton, C., "NASA's Advanced Space Transportation Hypersonic Program," *11th AIAA/AAAF International Conference Space Planes and Hypersonics Systems and Technologies Conference*, AIAA Paper 2002-5175, Sept.-Oct. 2002.
- [14] Hueter, U., "NASA's Next Generation Launch Technology Program - Strategy and Plans," *Proceedings of the 54th International Astronautical Congress of the International Astronautical Federation, the International Academy of Astronautics, and the International Institute of Space Law*, IAC Paper 2003-V.5.01, Sept.-Oct. 2003.
doi:10.2514/6.IAC-03-V.5.01
- [15] "Report on Why and Whither Hypersonic Research in the US Air Force," U.S. Air Force Scientific Advisory Board TR-00-03, Washington, D.C., Dec. 2003, pp. 77-92.
- [16] Bilardo, V., Hunt, J., Lovell, N., Maggio, G., Wilhite, A., and McKinney, L., "The Benefits of Hypersonic Airbreathing Launch Systems for Access to Space," *39th AIAA/ASME/SAE/ASEE Joint Propulsion Conference and Exhibit*, AIAA Paper 2003-5265, July 2003.
- [17] Culbertson, A., and Bhat, B., "The National Aerospace Initiative (NAI): Technologies for Responsive Space Access," <http://ntrs.nasa.gov/archive/nasa/casi.ntrs.nasa.gov/20030107848.pdf> [retrieved 15 April 2015].
- [18] McClinton, C., Rausch, V., Shaw, R., Mehta, U., and Naftel, C., "Hyper-X: Foundation for Future Hypersonic Launch Vehicle," *Acta Astronautica*, Vol. 57, Nos. 2-8, 2005, pp. 614-622.
doi:10.1016/j.actaastro.2005.03.061
- [19] McClinton, C., "X-43-Scramjet Power Breaks the Hypersonic Barrier, Dryden Lectureship in Research for 2006," *44th AIAA Aerospace Sciences Meeting and Exhibit*, AIAA Paper 2006-0001, Jan. 2006.
- [20] Dolvin, D., "Hypersonic International Flight Research and Experimentation," *16th AIAA/DLR/DGLR International Space Planes and Hypersonic Systems and Technologies Conference*, AIAA Paper 2009-7228, 2009.
- [21] Jackson, K., Gruber, M., and Buccellato, S., "HiFiRE Flight 2 - A Program Overview," *51st AIAA Aerospace Sciences Meeting*, AIAA Paper 2013-0695, Jan. 2013.
- [22] Mehta, U., "Strategy for Developing Air-Breathing Aerospace Plane," *Journal of Aircraft*, Vol. 33, No. 4, March-April 1996, pp. 377-385.
doi:10.2514/3.56938
- [23] Bowcutt, K., and Smith, T., "Responsive and Affordable Launch of Small Satellites: A Reusable Air-Breathing Concept," *AIAA Reinventing Space Conference*, AIAA Paper 2012-5001, 2012.
- [24] "Small Launch Vehicle," U.S. Patent 20130299626 A1, Boeing Company, Seattle, WA, Nov. 2013.
- [25] Mehta, U., Bowles, J., Pandya, S., Melton, J., Huynh, L., Kless, J., and Hawke, V., "Conceptual Stage Separation from Widebody Subsonic Carrier Aircraft for Space Access," *Aeronautical Journal*, Vol. 118, No. 1209, Nov. 2014, pp. 1279-1309.
- [26] Cowing, K., "Paul Allen Announces Revolution in Space Transportation Stratolaunch System," Dec. 2011, <http://spaceref.com/onorbit/paul-allen-announces-revolution-in-space-transportation-stratolaunch-system.html> [retrieved 14 Dec. 2011].
- [27] "Satellite Launch," Virgin Galactic, Pasadena, CA, <http://www.virgingalactic.com/satellite-launch> [retrieved 10 April 2015].
- [28] Hannigan, R. J., "Sänger: A Lead Concept," *Spaceflight in the Era of Aero-Space Planes*, Krieger, Malabar, FL, 1994, pp. 121-135.
- [29] "Aerospace Plane Technology, Research and Development Efforts in Europe," U.S. General Accounting Office Rept. GAO/NSIAD-91-194, Washington, D.C., July 1991.
- [30] Heitmer, F., Lederer, R., Voss, N., Bissinger, N., and Hermann, O., "Turboramjets and Installation," *Developments in High-Speed-Vehicle Propulsion Systems*, edited by Murthy, S. N. B., and Curran, E. T., Vol. 165, Progress in Astronautics and Aeronautics, AIAA, Reston, VA, 1996.
- [31] "Saenger II," *Encyclopedia Astronautica*, <http://www.astronautix.com/lvs/saengerii.htm> [retrieved 3 April 2015].
- [32] Li, A., "Critical Areas NASA Needs to Address in Managing Its Reusable Launch Vehicle Program," U.S. General Accounting Office Rept. GAO-01-826T, June 2011.
- [33] Cast, J., and Amatore, D., "NASA Reaches Milestone In Space Launch Initiative Program; Also Announces No SLI Funding for X-33 or X-34," NASA Headquarters, March 2001.
- [34] Bond, A., *Spaceflight in the Era of Aero-Space Planes*, edited by Hannigan, R. J., Krieger, Malabar, FL, 1994, pp. 102-103.
- [35] Varvill, R., and Bond, A., "The Skylon Spaceplane: Progress to Realization," *Journal of the British Interplanetary Society*, Vol. 61, 2008, pp. 412-418.
- [36] *SKYLON Users' Manual*, Reaction Engines, SKY-REL-MA-0001, Rev. 2.1, Abingdon, U.K., June 2014.
- [37] Varvill, R., and Bond, A., "A Comparison of Propulsion Concepts for SSTO Reusable Launchers," *Journal of the British Interplanetary Society*, Vol. 56, 2003, pp. 108-117.
- [38] Webber, H., Feast, S., and Bond, A., "Heat Exchanger Design in Combined Cycle Engines," *Proceedings of the 59th International Astronautical Congress*, International Astronautical Federation IAC-08.C4.5.1, Vol. 10, 2008, p. 6522.
- [39] Varvill, R., "Heat Exchanger Development at Reaction Engines Ltd.," *Acta Astronautica*, Vol. 66, 2010, pp. 1468-1474.
doi:10.1016/j.actaastro.2009.11.010
- [40] "The Biggest Breakthrough in Propulsion Since the Jet Engine," Reaction Engines Press Release, Nov. 2012.
- [41] "Heat Exchangers," U.S. Patent No. 2015/0101334 A1, Reaction Engines, April 2015.
- [42] Mehta, U., "Revolutionary Space Transportation Needed," *Space News*, Vol. 16, No. 18, May 2005, p. 19.
- [43] Mehta, U., "Future of Human Spaceflight," *Space News*, Vol. 20, No. 34, Aug. 2009, p. 19.
- [44] Chase, R., and Tang, M., "The Quest for a Robust, Responsive, Reliable, Efficient and Low Cost Space Access Capability," *16th AIAA/DLR/DGLR International Space Planes and Hypersonic Systems and Technologies Conference*, AIAA Paper 2009-7417, 2009.
- [45] Barth, T., Eggers, T., Ditttrich, R., and Otto, H., "Analysis of the Hypersonic Flow Field Around the Skylon Vehicle," Inst. of Aerodynamic and Flow Technology, Deutsches Zentrum für Luft- und Raumfahrt, DLR Technical Rept. IB-124-2011/907, Brunswick, Germany, Dec. 2011.
- [46] "Skylon Assessment Report," European Space Research and Technology Centre, European Space Agency TEC-MPC/2011/946/MF, No. 1, Rev. 2, Noordwijk, The Netherlands, June 2011.
- [47] Eggers, T., "Numerical Investigation on the Potential of Steam Cooling for the Skylon Spaceplane in Hypersonic Flow," *28th International Congress of the Aeronautical Sciences (ICAS)*, Inst. for Applied Mathematics and Computer Sciences Paper 2012-2.8.1, Brisbane, Australia, Sept. 2012.
- [48] Ahmad, A., Maddock, C., Scanlon, T., and Brown, R., "Prediction of the Aerodynamic Performance of Re-Usable Single Stage to Orbit Vehicles," *Proceedings of Space Access 2011*, Paris, Sept. 2011.
- [49] Wuilbercq, R., Ahmad, A., Scanlon, T., and Brown, R., "Towards Robust Aero-Thermodynamic Predictions for Re-Usable Single-Stage to Orbit Vehicles," *18th AIAA/3AF International Space Planes and Hypersonic Systems and Technologies Conference*, AIAA Paper 2012-5803, Sept. 2012.
- [50] Wuilbercq, R., Pescetelli, F., Minisci, E., and Brown, R., "Influence of Boundary Layer Transition on the Trajectory Optimization of a Reusable Launch Vehicle," *19th AIAA International Space Planes and Hypersonic Systems and Technologies Conference*, AIAA Paper 2014-2362, 2014.
- [51] Aftosmis, M. J., "Solution Adaptive Cartesian Grid Methods for Aerodynamic Flows with Complex Geometries," Lecture Series: 1997-02, von Karman Inst. for Fluid Dynamics, Brussels, March 1997.
- [52] Aftosmis, M. J., Berger, M. J., and Melton, J. E., "Robust and Efficient Cartesian Mesh Generation for Component-Based Geometry," *AIAA Journal*, Vol. 36, No. 6, June 1998, pp. 952-960.
doi:10.2514/2.464
- [53] van Leer, B., "Flux-Vector Splitting for the Euler Equations," Inst. for Applied Mathematics and Computer Sciences Paper 82-30, Sept. 1982.
- [54] Aftosmis, M. J., Berger, M. J., and Adomavicius, G. D., "A Parallel Multilevel Method for Adaptively Refined Cartesian Grids with Embedded Boundaries," *38th Aerospace Sciences Meeting and Exhibit*, AIAA Paper 2000-0808, 2000.
- [55] Aftosmis, M. J., Berger, M. J., and Murman, S. M., "Applications of Space-Filling-Curves to Cartesian Methods in CFD," *42nd AIAA Aerospace Sciences Meeting and Exhibit*, AIAA Paper 2004-1232, Jan. 2004.
- [56] Berger, M. J., Aftosmis, M. J., and Murman, S. M., "Analysis of Slope Limiters on Irregular Grids," *43rd AIAA Aerospace Sciences Meeting and Exhibit*, AIAA Paper 2005-0490, Jan. 2005.
- [57] Nemec, M., and Aftosmis, M. J., "Adjoint Sensitivity Computations for an Embedded-Boundary Cartesian Mesh Method," *Journal of Computational Physics*, Vol. 227, No. 4, 2008, pp. 2724-2742.
doi:10.1016/j.jcp.2007.11.018
- [58] "1976 Standard Atmosphere Calculator," <http://www.digitaldutch.com/atmoscalc>.

- [59] Venditti, D. A., and Darmofal, D. L., "Grid Adaptation for Functional Outputs: Application to Two-Dimensional Inviscid Flow," *Journal of Computational Physics*, Vol. 176, 2002, pp. 40–69.
doi:10.1006/jcph.2001.6967
- [60] Aftosmis, M. J., and Berger, M. J., "Multilevel Error Estimation and Adaptive h-Refinement for Cartesian Meshes with Embedded Boundaries," *40th AIAA Aerospace Sciences Meeting and Exhibit*, AIAA Paper 2002-0863, 2002.
- [61] Nemec, M., and Aftosmis, M. J., "Toward Automatic Verification of Goal-Oriented Flow Simulations," NASA TM-2014-218386, 2014.
- [62] Sutton, G., and Biblarz, O., "Real Nozzles," *Rocket Propulsion Elements*, 7th ed., John Wiley & Sons, New York, 2001, pp. 85–92.
- [63] Pindzola, M., "Jet Simulation in Ground Test Facilities," AGARDograph-79, Neuilly sur Seine, France, Nov. 1963.
- [64] Brauckmann, G., Greathouse, J., and White, M., "Rocket Plume Scaling for Orion Wind Tunnel Testing," *29th AIAA Applied Aerodynamics Conference*, AIAA Paper 2011-3341, June 2011.
- [65] Chaderjian, N., Rogers, S., Aftosmis, M., Pandya, S., Ahmad, J., and Tejnil, E., "Automated Euler and Navier–Stokes Database Generation for a Glide-Back Booster," *Proceedings of the 3rd International Conference on Computational Fluid Dynamics*, edited by Groth, C., and Zingg, D., Springer-Verlag, Berlin, July 2004, pp. 251–256.
- [66] Jespersen, D., Pulliam, T., and Buning, P., "Recent Enhancements to Overflow," *35th Aerospace Sciences Meeting and Exhibit*, AIAA Paper 1997-0644, Jan. 1997.
- [67] Brandis, A., Wray, A., Liu, Y., Schwenke, D., Carbon, D., Huo, W., and Johnston, C., "Validation of HyperRad for Earth Entries," *44th AIAA Thermophysics Conference*, AIAA Paper 2013-2777, 2013.
- [68] Gusman, M., Housman, J., and Kiris, C., "Best Practices for CFD Simulations of Launch Vehicle Ascent with Plumes—OVERFLOW Perspective," *49th AIAA Aerospace Sciences Meeting*, AIAA Paper 2011-1054, Jan. 2011.

M. Miller
Associate Editor